Electrocatalysis Hot Paper

How to cite: *Angew. Chem. Int. Ed.* **2023,** *62,* e202218728
International Edition: doi.org/10.1002/anie.202218728
German Edition: doi.org/10.1002/ange.202218728

Alternating Metal-Ligand Coordination Improves Electrocatalytic CO_2 Reduction by a Mononuclear Ru Catalyst**

Hemlata Agarwala[+], Xiaoyu Chen[+], Julien R. Lyonnet, Ben A. Johnson, Mårten Ahlquist,* and Sascha Ott**

Abstract: Molecular electrocatalysts for CO_2-to-CO conversion often operate at large overpotentials, due to the large barrier for C–O bond cleavage. Illustrated with ruthenium polypyridyl catalysts, we herein propose a mechanistic route that involves one metal center that acts as both Lewis base and Lewis acid at different stages of the catalytic cycle, by density functional theory in corroboration with experimental FTIR. The nucleophilic character of the Ru center manifests itself in the initial attack on CO_2 to form $[\mathbf{Ru}\text{-}CO_2]^0$, while its electrophilic character allows for the formation of a 5-membered metallacyclic intermediate, $[\mathbf{Ru}\text{-}CO_2CO_2]^{0,c}$, by addition of a second CO_2 molecule and intramolecular cyclization. The calculated activation barrier for C–O bond cleavage via the metallacycle is decreased by 34.9 kcal mol^{-1} as compared to the non-cyclic adduct in the two electron reduced state of complex **1**. Such metallacyclic intermediates in electrocatalytic CO_2 reduction offer a new design feature that can be implemented consciously in future catalyst designs.

Introduction

Electrochemical reduction of CO_2 can assist in mitigating atmospheric CO_2 levels and offer scalable means to store renewable electricity in energy dense compounds such as CO. Unfortunately, the electrochemical conversion of CO_2 to CO typically suffers from high overpotentials that impede efficient implementation.[1–3] In molecular transition metal-based catalysts, three key steps have been identified as potential kinetic bottlenecks: 1) CO_2 binding to the catalyst that is accompanied by bending of linear CO_2, 2) cleavage of a C–O bond in the $[\text{metal-}CO_2]^{n+}$ adduct and 3) CO dissociation from the catalyst. Of these three steps, the current report focuses mainly on C–O bond cleavage in molecular catalysts. Multiple electrochemical reduction steps to form a low-valent pre-catalytic state have been shown to facilitate this process, but these typically occur at more negative standard potentials, thus leading to high overpotentials.[4–10] In nature, carbon monoxide dehydrogenase enzymes (CODH) can efficiently and reversibly convert CO to CO_2.[11] In the active site of CODH from the anaerobic bacterium *C. hydrogenoformans*, there is a [Ni-4Fe-5S] cluster, called the *C*-cluster, which consists of a [Ni-3Fe-4S] cubane linked to a unique Fe site through a sulfide.[12,13] In this cluster, Ni is the redox active center to which CO_2 binds. In close proximity is a redox inactive Fe^{III} Lewis acid that facilitates C–O cleavage by stabilizing the OH^- group formed during the process.[13] Efforts to mimic this function in artificial systems include the simple addition of Brønsted acids to enhance catalytic activity.[4,5,7,10,14–36] Also, several metal complexes with intramolecular Brønsted

[*] Dr. H. Agarwala,[+] J. R. Lyonnet, Dr. B. A. Johnson, Prof. Dr. S. Ott
Department of Chemistry - Ångström Laboratories, Uppsala University
Box 523, 75120 Uppsala (Sweden)
E-mail: hemlataagarwala@gmail.com
sascha.ott@kemi.uu.se
Homepage: https://ebt.cs.tum.de/team/?lang=en
https://www.kemi.uu.se/angstrom/research/synthetic-molecular-chemistry/research-groups/ott-group/

Dr. H. Agarwala,[+] Dr. B. A. Johnson
Present address: Technical University of Munich (TUM), Campus Straubing for Biotechnology and Sustainability
Uferstraße 53, 94315 Straubing (Germany)
E-mail: hemlata.agarwala@tum.de

X. Chen,[+] Prof. Dr. M. Ahlquist
Department of Theoretical Chemistry and Biology, School of Engineering Sciences in Chemistry, Biotechnology and Health (CBH), KTH Royal Institute of Technology
10691 Stockholm (Sweden)
E-mail: ahlqui@kth.se
Homepage: https://www.kth.se/profile/ahlqui/page/group?l=en

J. R. Lyonnet
Present address: Institute of Chemical Research of Catalonia (ICIQ), The Barcelona Institute of Science and Technology
43007 Tarragona (Spain)

[+] These authors contributed equally to this work.

[**] A previous version of this manuscript has been deposited on a preprint server (https://doi.org/10.26434/chemrxiv.14035625.v2).

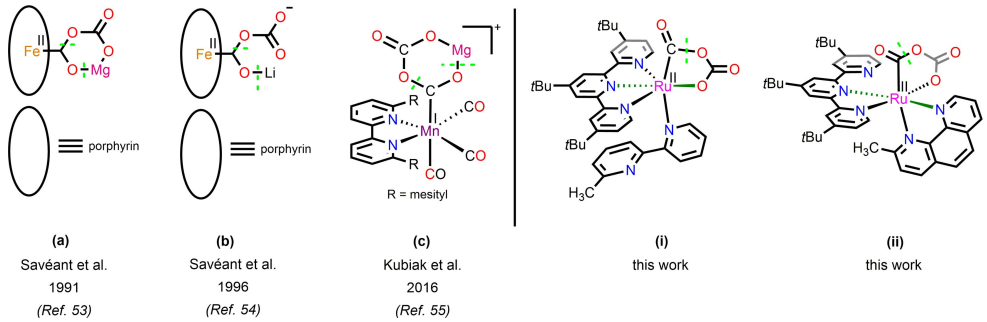

Figure 1. Representations of some transition metal-bound CO_2 adducts: (a–c) previously proposed,[53–55] stabilized by Lewis acid (LA) cations like Mg^{2+} and Li^{+}; (i and ii) investigated in the present work. The dashed green lines (····) indicate the scission of C–O and O–LA bonds in the subsequent step of the respective catalytic cycles.

acidic groups positioned close to the reactive center have been shown to facilitate C–O cleavage.[3,10,29,35,37–52]

Examples of catalytic rate enhancements for CO_2 electroreduction by Lewis acidic metal ions in molecular catalysts are comparatively rare.[32,53–55] In some of these systems, cyclic intermediates that comprise the catalytic metal center, two molecules of CO_2 and an exogenous alkali or alkaline earth metal Lewis acid have been proposed[53–55] (Figures 1a–1c); however, to the best of our knowledge, none was observed experimentally. It has been postulated that C–O cleavage from these cyclic intermediates is more facile compared to the systems without the additional Lewis acid. Herein, we report a unique pathway for C–O bond cleavage in the overall reductive disproportionation of CO_2 to CO and CO_3^{2-} that requires neither excessive catalyst reductions nor external Lewis acids. The mechanistic route involves *one* metal center that acts as both Lewis base and Lewis acid at different stages of the catalytic cycle. The pathway is enabled by the flexible ligation of polypyridine ligands that can liberate open coordination sites (Figures 1-(i) and 1(ii)).

Results and Discussion

The aforementioned mechanism is exemplified by two Ru-based catalysts, $[Ru(tBu_3tpy)(CH_3bpy)(CH_3CN)]^{2+}$ ($\mathbf{1}^{2+}$)[56,57] and $[Ru(tBu_3tpy)(CH_3phen)(CH_3CN)]^{2+}$ ($\mathbf{2}^{2+}$) (Scheme 1; tBu_3tpy = 4,4′,4″-tri-*tert*-butyl-2,2′:6′,2″-terpyridine; CH_3bpy = 6-methyl-2,2′-bipyridine, CH_3phen = 2-methyl-1,10-phenanthroline) that differ in the bidentate ligand motif. The bidentate CH_3phen in $\mathbf{2}^{2+}$ is a structurally more rigid ligand due to the fusion of the two pyridine rings,[58,59] rendering the ligand less prone to distortion, than CH_3bpy in $\mathbf{1}^{2+}$. The presence of the methyl group *ortho* to the nitrogen in the bidentate ligand is motivated by our previous finding that it labilizes the coordinated CH_3CN upon one-electron reduction of the complex.[56]

Complexes $\mathbf{1}^{2+}$ and $\mathbf{2}^{2+}$ were prepared from $Ru^{III}(tBu_3tpy)(Cl)_3$ and the respective bidentate ligand by slight modifications of published procedures[56] (see Experimental Section, and Figures S1 and S2, in Supporting Information).

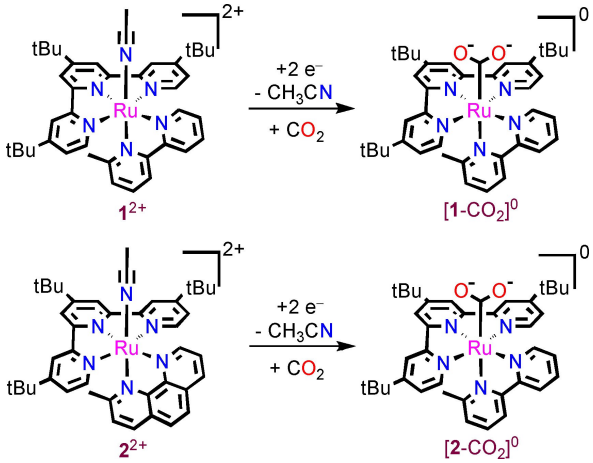

Scheme 1. Pictorial representation of complexes $\mathbf{1}^{2+}$ and $\mathbf{2}^{2+}$, and their two-electron reduced CO_2 adducts $[\mathbf{1}\text{-}CO_2]^0$ and $[\mathbf{2}\text{-}CO_2]^0$, respectively.

As mentioned above, owing to the *ortho* methyl groups of the bidentate ligand, both complexes can liberate the CH_3CN ligand upon one-electron reduction.[56] The coordinatively unsaturated intermediate acts as a Lewis base towards CO_2, ultimately leading to the two-electron reduced CO_2 adducts $[\mathbf{1}\text{-}CO_2]^0$ and $[\mathbf{2}\text{-}CO_2]^0$ (Scheme 1)[56] which are the starting points of the present study.

The cyclic voltammograms (CVs) of complexes $\mathbf{1}^{2+}$ and $\mathbf{2}^{2+}$ show electrochemically reversible one-electron reductions under argon at −1.76 V and −1.77 V versus $Fc^{+/0}$ respectively (Figure 2, Table S1), the cathodic peak potential being −1.81 V (versus $Fc^{+/0}$) for both.

The corresponding DFT calculated standard potentials of −1.84 V and −1.81 V versus $Fc^{+/0}$ for $\mathbf{1}^{2+}$ and $\mathbf{2}^{2+}$ respectively, match well with the experimental values (See Computational details and Table S0 in Supporting Information). Linear variation of peak currents with the square root of the scan rate for the first reduction of $\mathbf{2}^{2+}$ under argon (Figure S3) reveals diffusion-controlled behavior, with the diffusion coefficient (D) being 8.11×10^{-6} cm^2s^{-1} (details of calculation of D can be found under Figure S3 in Supporting Information).

Upon addition of CO_2 (0.28 M),[60] the first reductions become irreversible with noticeable enhancement in catho-

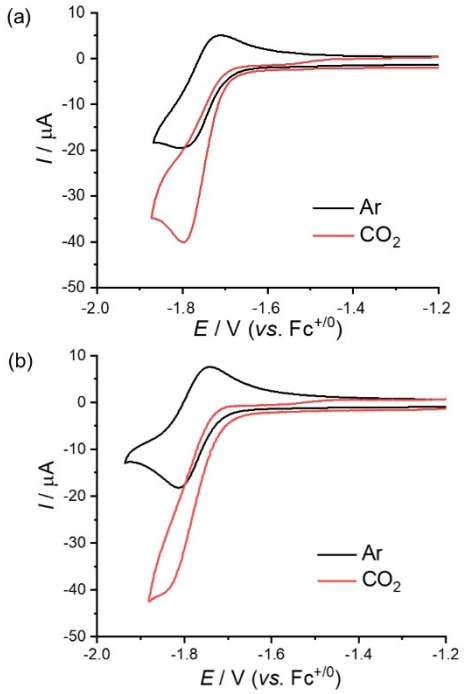

Figure 2. Cyclic voltammograms (shown is the first reduction) under Ar (black) and CO_2 (red; 0.28 M) of 1.0 mM solutions of (a) $\mathbf{1}(PF_6)_2$ and (b) $\mathbf{2}(PF_6)_2$. $\nu = 0.1\ V s^{-1}$, CH_3CN/0.1 M $TBAPF_6$.

dic current, indicative of the electrochemical disproportionation of CO_2 to CO and CO_3^{2-}.[61,56] This was confirmed by the observation of peaks for CO and CO_3^{2-} in the Fourier transformed infra-red (FT-IR) spectrum recorded at the end of a controlled potential electrolysis (CPE) of a CO_2 saturated solution of $\mathbf{2}(PF_6)_2$ in anhydrous CH_3CN (Figure S4).

As discussed above, C–O bond cleavage is one of the kinetic bottlenecks in CO_2 reduction chemistry, and mechanistic details of this step have hitherto been elusive for $[\mathbf{1}\text{-}CO_2]^0$ and $[\mathbf{2}\text{-}CO_2]^0$. DFT calculations estimate the standard potential for the $[\mathbf{1}\text{-}CO_2]^{-1}/[\mathbf{1}\text{-}CO_2]^0$ couple to be −2.43 V (versus $Fc^{+/0}$), which is substantially more negative than the applied potential of −1.82 V (versus $Fc^{+/0}$), the experimental potential of interest in the present study (Figure 2). Hence, the addition of a third electron to $[\mathbf{1}\text{-}CO_2]^0$ is ruled out. Alternatively, $[\mathbf{1}\text{-}CO_2]^0$ could be envisaged to dimerize via the interaction between the negatively charged oxygen on one molecule and the partial positive charge on the CO_2 carbon of a second molecule. DFT optimization to obtain such a structure resulted in the two molecules moving apart (Figure S5). Such a behavior can be attributed to the steric encumbrance between the bulky *tert*-butyl groups on the terpyridine ligands of the two molecules. Hence, the dimerization of $[\mathbf{1}\text{-}CO_2]^0$ as a possibility is also discarded.

It is well documented for related systems that in the absence of any exogenous Lewis acids such as protons or metal salts, the oxygen of the metal-bound CO_2 is sufficiently nucleophilic to attack a second CO_2 molecule.[55–57,61]

DFT calculations show that for the pre-catalysts $\mathbf{1}^{2+}$ and $\mathbf{2}^{2+}$, this occurs at the two-electron reduced state, thereby producing $[\mathbf{1}\text{-}CO_2CO_2]^0$ and $[\mathbf{2}\text{-}CO_2CO_2]^0$ from $[\mathbf{1}\text{-}CO_2]^0$ and $[\mathbf{2}\text{-}CO_2]^0$, respectively (Figures 3 and 4). The activation energy (ΔG^{+}) for this step is calculated to be 14.1 kcal mol^{-1} and 10.9 kcal mol^{-1} for $[\mathbf{1}\text{-}CO_2]^0$ and $[\mathbf{2}\text{-}CO_2]^0$, respectively, with corresponding reaction free energies of 6.0 kcal mol^{-1} and 4.1 kcal mol^{-1}. While $[\mathbf{1}\text{-}CO_2CO_2]^0$ is a plausible intermediate in the catalytic cycle, direct C–O bond cleavage to produce CO_3^{2-} and the carbonyl complex (Scheme S2(a)) is not a viable option, as the calculated ΔG^{+} for this reaction is extremely high (59.3 kcal mol^{-1}).

Alternatively, the negatively charged terminal oxygen in $[\mathbf{1}\text{-}CO_2CO_2]^0$ could be envisaged to attack the Ru center of a 5-coordinate intermediate, $\mathbf{1}^{+}$, that is obtained by the dissociation of CH_3CN from the one-electron reduced six-coordinate $[\mathbf{1}\text{-}CH_3CN]^{+}$,[56] leading to the formation of a

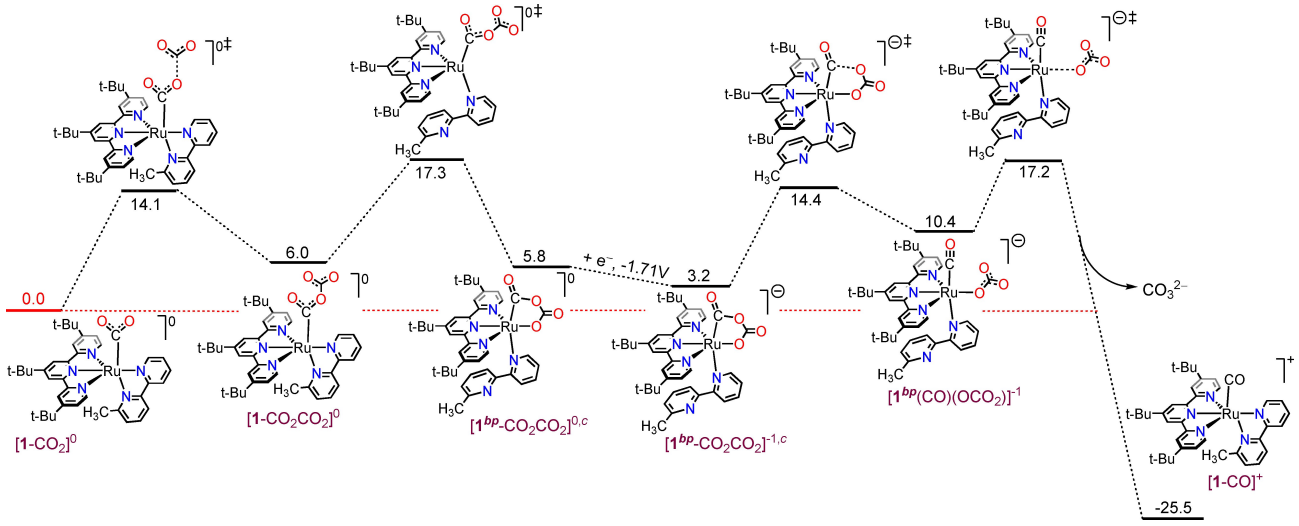

Figure 3. DFT calculated pathway from $[\mathbf{1}\text{-}CO_2]^0$ to CO_3^{2-} via the cyclic three-electron reduced intermediate $[\mathbf{1}^{bp}\text{-}COOCO_2]^{-1,c}$ at an applied potential of −1.82 V versus $Fc^{+/0}$ in CH_3CN.

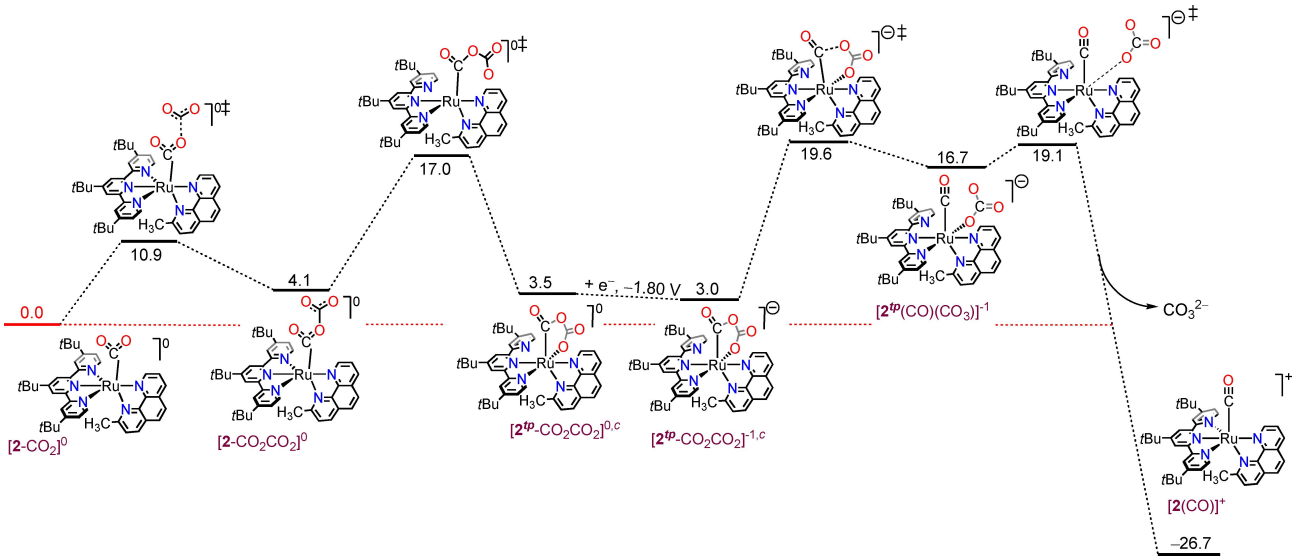

Figure 4. DFT calculated pathway from [**2**-CO_2]^0 to CO_3^{2-} via the cyclic three-electron reduced intermediate [$\mathbf{2}^{tp}$-CO_2CO_2]$^{-1,c}$ at an applied potential of −1.82 V versus $Fc^{+/0}$ in CH_3CN.

bimetallic intermediate with a –C(O)O–C(O)O– bridge (Scheme S2(b)), similar to the one proposed for Re^I(bpy)-$(CO)_3X$ catalysts.[62–64] However, the presence of $\mathbf{1}^+$ at an applied potential of −1.82 V (versus $Fc^{+/0}$) is not possible, as the standard potential for the $\mathbf{1}^+/\mathbf{1}^0$ couple is calculated to be −1.66 V (versus $Fc^{+/0}$), showing the facile formation of $\mathbf{1}^0$. The reaction free energy for the attack of [**1**-CO_2CO_2]^0 onto the 5-coordinate $\mathbf{1}^0$ instead, to form a similar bimetallic intermediate (Scheme S2(c)), was calculated to be 31.0 kcal mol^{-1} with respect to [**1**-CO_2]^0. This route is also ruled out in comparison to a lower energy pathway, as described in the following section.

In the absence of any other established literature pathway, we hypothesized whether a structural reorganization of the complex, either to facilitate C–O bond cleavage or to drive a third reduction at a more positive potential, could provide an energetically plausible pathway. A closer inspection of [**1**-CO_2CO_2]^0 shows that both –CO_2CO_2 and -CH_3bpy are bidentate ligands. Hence, the possibility of a ligand exchange between the equatorial pyridine of CH_3bpy and the terminal oxygen of -CO_2CO_2 to form [$\mathbf{1}^{bp}$-CO_2CO_2]^{0,c} (Figure 3) was explored. The reaction was found to have a $\Delta G^{\ddagger}$ of 11.3 kcal mol^{-1}, with [$\mathbf{1}^{bp}$-CO_2CO_2]^{0,c} being more stable than [**1**-CO_2CO_2]^0 by merely 0.2 kcal mol^{-1} (Figure 3). The C–O bond that needs to be cleaved is elongated from 1.28 Å (in [**1**-CO_2CO_2]^0) to 1.44 Å (in [$\mathbf{1}^{bp}$-CO_2CO_2]^{0,c}), indicating enhanced single bond character. Cyclic 5-membered metallacycles of this kind are not entirely unprecedented, and have been reported in the reaction of low-valent metal species with CO_2, albeit in a *stoichiometric* fashion (Figure S6).[65–71] In context of catalytic CO_2 conversion, a related Co-based metallacycle was recently proposed by Lloret-Fillol and co-workers, however without any experimental evidence or support.[6] Partial de-coordination of polydentate polypyridyl ligands from metal centers upon reduction have also been postulated earlier by some groups.[72–74] However, the synergistic occurrence of these two processes in a single catalytic framework is, to the best of our knowledge, unprecedented. An alternative ligand exchange between a terminal pyridine of tBu$_3$tpy and the terminal oxygen of -CO_2CO_2 in [**1**-CO_2CO_2]^0 to form [$\mathbf{1}^{tp}$-CO_2CO_2]^{0,c} (Figure S7) was found to have a $\Delta G^{\ddagger}$ of 19.6 kcal mol^{-1} with [$\mathbf{1}^{tp}$-CO_2CO_2]^{0,c} being less stable than [**1**-CO_2CO_2]^0 by 4.7 kcal mol^{-1}. Therefore, this pathway would be less preferred over the decoordination of the equatorial pyridine of CH_3bpy as seen from the energetics above.

Another interesting aspect of the cyclic intermediate [$\mathbf{1}^{bp}$-CO_2CO_2]^{0,c} is that the intramolecular Lewis acid stabilization of the negative charge at the terminal O by the Ru center facilitates another reduction step from [$\mathbf{1}^{bp}$-CO_2CO_2]^{0,c} to [$\mathbf{1}^{bp}$-CO_2CO_2]$^{-1,c}$. The potential for this reduction was calculated to be −1.71 V (versus $Fc^{+/0}$ in CH_3CN) (Figure 3), which is 110 mV more positive than the experimental applied potential of −1.82 V.[56]

The occurrence of [$\mathbf{1}^{bp}$-CO_2CO_2]$^{-1,c}$ as an intermediate, prompted us to investigate an alternative pathway where the [**1**-CO_2CO_2]^0 intermediate, instead of undergoing intramolecular cyclization, is reduced by another electron to further weaken the aforementioned C–O bond, hence forming the intermediate [**1**-CO_2CO_2]$^{-1}$ (Figure S8). DFT calculations predict this redox process to occur at a standard potential of −2.06 V (versus $Fc^{+/0}$), which is 240 mV more negative than the applied potential of −1.82 V (versus $Fc^{+/0}$) under consideration[56] (Figure S8). The potential of −2.06 V translates to a reaction free energy of 5.5 kcal mol^{-1}, which is 5.8 kcal mol^{-1} lower than the activation free energy for the conversion of [**1**-CO_2CO_2]^0 to [$\mathbf{1}^{bp}$-CO_2CO_2]^{0,c}. The subsequent cyclization of [**1**-CO_2CO_2]$^{-1}$ proceeds with an activation barrier of 7.4 kcal mol^{-1} to ultimately result in [$\mathbf{1}^{bp}$-CO_2CO_2]$^{-1,c}$ (Figure S8). This barrier converts to a rate constant that is about three orders of magnitude higher than the rate constant for intramolecular cyclization of [**1**-

$CO_2CO_2]^0$ (details of this calculation can be found under Figure S8). However, the 240 mV difference between the standard potential for the [**1**-$CO_2CO_2]^{-1}$/[**1**-$CO_2CO_2]^0$ couple and the applied potential, results in the concentration of [**1**-$CO_2CO_2]^{-1}$ being four orders of magnitude lower than that of [**1**-$CO_2CO_2]^0$ (calculations under Figure S8). Therefore, considering the cyclization to be a first order reaction, this difference in concentrations, combined with the relative rate constants of cyclization, leads to an overall apparent rate of formation of [$\mathbf{1}^{bp}$-$CO_2CO_2]^{-1,c}$ through [$\mathbf{1}^{bp}$-$CO_2CO_2]^{0,c}$ to be about 13 times faster than through [**1**-$CO_2CO_2]^{-1}$ (calculations under Figure S8). This difference in the relative rates implies that both the competing pathways to form [$\mathbf{1}^{bp}$-$CO_2CO_2]^{-1,c}$ from [**1**-$CO_2CO_2]^0$ are operational at −1.82 V (versus $Fc^{+/0}$), however to different extents.

Having identified the different pathways leading to [$\mathbf{1}^{bp}$-$CO_2CO_2]^{-1,c}$, we dived into the possibility of C–O bond cleavage in this intermediate. Its DFT optimized structure reveals its similarity to that of [$\mathbf{1}^{bp}$-$CO_2CO_2]^{0,c}$, with a relatively long C–O bond (1.45 Å) that is to be cleaved. The formation of the metallacycle also induces some strain, that further weakens the C–O bond, as evidenced by the small O–Ru–C angle of 80.0° in [$\mathbf{1}^{bp}$-$CO_2CO_2]^{-1,c}$. The transition state for C–O cleavage was located just 11.2 kcal mol^{-1} above [$\mathbf{1}^{bp}$-$CO_2CO_2]^{-1,c}$, resulting in [$\mathbf{1}^{bp}$(CO)(OCO_2)]$^{-1}$ at 10.4 kcal mol^{-1} relative to [**1**-$CO_2]^0$. Dissociation of carbonate then proceeds with an activation energy at 17.2 kcal mol^{-1} relative to [**1**-$CO_2]^0$, accompanied by restoration of the bidentate coordination mode of CH_3bpy to Ru to form [**1**-CO]$^+$ (Figure 3). The highest activation energy barriers ($\Delta G^{\ddagger}$) in the pathway (Figure 3) are for the formation of [$\mathbf{1}^{bp}$-$CO_2CO_2]^{0,c}$ at 17.3 kcal mol^{-1} and the release of carbonate at a similar free energy ($\Delta G^{\ddagger}$ relative to [**1**-$CO_2]^0$) of 17.2 kcal mol^{-1}. The barriers agree well with the experimental maximum turnover frequency (TOF_{max})[57] of 1.8 s^{-1} which corresponds to an activation free energy of 17.2 kcal mol^{-1} as obtained from Eyring equation[75] (see Supporting Information for details of this conversion).

Having identified the flexible coordination of the bidentate ligand and the subsequent formation of the [$\mathbf{1}^{bp}$-$CO_2CO_2]^{-1,c}$ metallacycle as crucial features for efficient C–O bond cleavage, focus was directed towards the 1,10-phenanthroline analogue [**2**-$CO_2]^0$ (Figure 4). Analogous to [**1**-$CO_2]^0$, it reacts with another CO_2 molecule to form the [**2**-$CO_2CO_2]^0$ intermediate, with an activation free energy of 10.9 kcal mol^{-1}, the reaction free energy being 4.1 kcal mol^{-1} (Figure 4).

The intramolecular cyclization in [**2**-$CO_2CO_2]^0$ by the attack of the terminal oxygen of –CO_2CO_2 onto Ru, to produce a metallacyclic intermediate analogous to that for complex $\mathbf{1}^{2+}$ was then investigated. Since the structure of CH_3phen is more rigid than CH_3bpy as mentioned earlier, the partial decoordination of CH_3phen from [**2**-$CO_2CO_2]^0$ (Figure 4) is expected to be more difficult than CH_3bpy. This is in fact the case, as the DFT optimization of the transition state (TS) for this process resulted in complete decoordination of CH_3phen from Ru (Figures S9(a) and S9(c)). The activation free energy for this process was calculated to be 22.2 kcal mol^{-1} with respect to [**2**-$CO_2]^0$ (Figure S9(d)), higher than the analogous activation barrier of 17.3 kcal mol^{-1} for the formation of [$\mathbf{1}^{bp}$-$CO_2CO_2]^{0,c}$ (Figure 3). The reaction free energy of the cyclic intermediate [$\mathbf{2}^{phen}$-$CO_2CO_2]^{0,c}$ (Figure S9(b)) was 4.0 kcal mol^{-1} (Figure S9(d)). The higher $\Delta G^{\ddagger}$ for the formation of [$\mathbf{2}^{phen}$-$CO_2CO_2]^{0,c}$ prompted us to find another pathway for the formation of a related cyclic intermediate, [$\mathbf{2}^{tp}$-$CO_2CO_2]^{0,c}$, achieved by liberation of one of the pyridine units of the tBu$_3$tpy ligand in [**2**-$CO_2CO_2]^0$ instead (Figure 4). The activation free energy for this cyclization step was calculated as 12.9 kcal mol^{-1}, with [$\mathbf{2}^{tp}$-$CO_2CO_2]^{0,c}$ being merely 0.6 kcal mol^{-1} lower in energy than [**2**-$CO_2CO_2]^0$. The difference of 9.3 kcal mol^{-1} in $\Delta G^{\ddagger}$ for the formation of [$\mathbf{2}^{phen}$-$CO_2CO_2]^{0,c}$ versus [$\mathbf{2}^{tp}$-$CO_2CO_2]^{0,c}$, indicates that the latter is preferred. These energies therefore show that replacement of -CH_3bpy with -CH_3phen has made the partial decoordination of tBu$_3$tpy more probable both kinetically and thermodynamically.

An interesting observation is the appreciable differences in activation free energy (19.6–12.9 = 6.7 kcal mol^{-1}) and free energy of formation (4.7 + 0.6 = 5.3 kcal mol^{-1}) of the metallacyclic intermediates [$\mathbf{1}^{tp}$-$CO_2CO_2]^{0,c}$ and [$\mathbf{2}^{tp}$-$CO_2CO_2]^{0,c}$, obtained by the partial decoordination of tBu$_3$tpy in [**1**-$CO_2CO_2]^0$ and [**2**-$CO_2CO_2]^0$ respectively, with [$\mathbf{1}^{tp}$-$CO_2CO_2]^{0,c}$ being higher in energy than [**1**-$CO_2CO_2]^0$.by 4.7 kcal mol^{-1}, whereas [$\mathbf{2}^{tp}$-$CO_2CO_2]^{0,c}$ is 0.6 kcal mol^{-1} lower than [**2**-$CO_2CO_2]^0$ (Figure S10(a)). These energy differences may be attributed to [**1**-$CO_2CO_2]^0$ being more polar than [**2**-$CO_2CO_2]^0$ as seen from their electrostatic potential maps on total electron density (Figures S10(b) and S10(c). The polarity differences arise from the fact that CH_3bpy is a better electron donor than CH_3phen.[76] The metallacyclic intermediates are however, similar in polarity due to the negative charge on the terminal oxygen being neutralised by the cationic Ru centre (Figures S10(d) and S10(e)). As expected on grounds of the polarity of the molecule, [**1**-$CO_2CO_2]^0$ is associated with a more negative solvation free energy than [**2**-$CO_2CO_2]^0$ (Table S2). Therefore, the difference in solvation free energies (ΔE_{solv}) between [**1**-$CO_2CO_2]^0$ and [$\mathbf{1}^{tp}$-$CO_2CO_2]^{0,c}$ is −27.74 kcal mol^{-1}, whereas between [**2**-$CO_2CO_2]^0$ to [$\mathbf{2}^{tp}$-$CO_2CO_2]^{0,c}$ it is −23.89 kcal mol^{-1} (Table S2). Hence, the difference of 3.85 kcal mol^{-1} {(−23.89)–(−27.74)}, in solvation free energy change, is what contributes to the difference in reaction free energies for partial decoordination of tBu$_3$tpy in complexes **1** and **2**. Another minor contribution perhaps comes from the fact that CH_3bpy is more susceptible towards structural distortion than CH_3phen. This leads to slightly more distorted structure of [$\mathbf{1}^{tp}$-$CO_2CO_2]^{0,c}$ as compared to [$\mathbf{2}^{tp}$-$CO_2CO_2]^{0,c}$ (Table S3), which in turn results in better overlap of orbitals in [$\mathbf{2}^{tp}$-$CO_2CO_2]^{0,c}$, as seen from the highest occupied molecular orbitals (HOMO) (Figures S10(f) and S10(g)).

In analogy to the situation in [$\mathbf{1}^{bp}$-$CO_2CO_2]^{0,c}$, the formation of the cyclic intermediate [$\mathbf{2}^{tp}$-$CO_2CO_2]^{0,c}$ allows access to a further reduction at a potential of −1.80 V (versus $Fc^{+/0}$) (Figure 4) that is slightly more positive than the first reduction. The result is the three-electron reduced, cyclic adduct [$\mathbf{2}^{tp}$-$CO_2CO_2]^{-1,c}$ which is found as the lowest

energy intermediate in the catalytic pathway (Figure 4), just before C–O bond cleavage.

The further reduction of $[\mathbf{2}\text{-}CO_2CO_2]^0$ to $[\mathbf{2}\text{-}CO_2CO_2]^{-1}$, followed by intramolecular cyclization of the latter to form $[\mathbf{2}^{tp}\text{-}CO_2CO_2]^{-1,c}$ was investigated as an alternative pathway (Figure S11). The reduction event was calculated to occur at −2.15 V (versus $Fc^{+/0}$), 330 mV more negative than the applied potential of −1.82 V (versus $Fc^{+/0}$). The cyclization of $[\mathbf{2}\text{-}CO_2CO_2]^{-1}$ to $[\mathbf{2}^{tp}\text{-}CO_2CO_2]^{-1,c}$ then proceeds with an activation free energy of 12.1 kcal mol^{-1}, which is merely 0.9 kcal mol^{-1} lower than the $\Delta G^{\ddagger}$ of 13.0 kcal mol^{-1} for the conversion of $[\mathbf{2}\text{-}CO_2CO_2]^0$ to $[\mathbf{2}^{tp}\text{-}CO_2CO_2]^{0,c}$ (Figure S11). These energies combined with the 330 mV difference in potentials result in an estimated apparent rate of this alternative pathway to be around seven orders of magnitude lower than that incorporating the intramolecular cyclization of $[\mathbf{2}\text{-}CO_2CO_2]^0$ followed by reduction (details of calculation under Figure S11). This striking difference in apparent rates rules out the pathway that passes through the reduction of $[\mathbf{2}\text{-}CO_2CO_2]^0$ to $[\mathbf{2}\text{-}CO_2CO_2]^{-1}$.

The relatively high computed stabilities of the cyclic intermediates $[\mathbf{1}^{bp}\text{-}CO_2CO_2]^{-1,c}$, $[\mathbf{2}^{tp}\text{-}CO_2CO_2]^{0,c}$ and $[\mathbf{2}^{tp}\text{-}CO_2CO_2]^{-1,c}$ indicate that their spectroscopic observation during electrocatalytic CO_2 reduction might be feasible. Hence, we resorted to infra-red (IR) spectroscopy. Experimentally, the relevant region in the infra-red (IR) spectra is convoluted by the evolution of three major bands at 1684 cm^{-1}, 1645 cm^{-1} and 1304 cm^{-1} that arise from the reductive disproportionation product CO_3^{2-} (Figures 5a and S12(a)); peaks are marked by asterisks *), as previously reported for $\mathbf{1}^{2+}$.[56,79] Similar spectral features are also observed in the experimental FT-IR spectra obtained from $\mathbf{2}^{2+}$ in the current study (Figures 5b and S12(b)).

A close inspection of the FT-IR spectra obtained during the controlled potential electrolysis (CPE) of a 1.0 mM solution of $\mathbf{1}^{2+}$ in anhydrous CH_3CN under CO_2 (0.28 M) (Figure 5a) reveals the evolution of a weak shoulder at 1740 cm^{-1} along with some convoluted transitions near 1230 cm^{-1}.[56] DFT calculations show that these two absorptions most likely arise from a symmetric and an asymmetric C=O stretching vibration (Figure S13(c)) that are however ambiguous to assign to one particular species.[78] Both $[\mathbf{1}\text{-}CO_2]^0$ (calc. at 1731 cm^{-1} and 1235 cm^{-1}; Figures S13(a)) and $[\mathbf{1}^{bp}\text{-}CO_2CO_2]^{-1,c}$ (calc. at 1759 cm^{-1} and 1235 cm^{-1}; Figure S13(b)) exhibit calculated IR vibrations that correspond well with the experimentally observed ones.

Furthermore, IR bands were observed at 2001, 1960 and 1932 cm^{-1} during CPE of $\mathbf{1}^{2+}$ (Figure S14) and at 2086, 2001 and 1932 cm^{-1} during CPE of $\mathbf{2}^{2+}$ (Figure S15) in anhydrous CH_3CN under CO_2 (0.28 M). These bands correspond very well with the DFT calculated IR spectral transitions at 2004, 1954 and 1925 cm^{-1} for $[\mathbf{1}\text{-}CO]^{2+}$, $[\mathbf{1}\text{-}CO]^{+}$, $[\mathbf{1}\text{-}CO]^0$ respectively (Figure S16), and at 2078, 2007, and 1925 cm^{-1} for $[\mathbf{2}\text{-}CO]^{2+}$, $[\mathbf{2}\text{-}CO]^{+}$, $[\mathbf{2}\text{-}CO]^0$ respectively (Figure S17). We were also able to observe the growth of the band for free CO in CH_3CN at 2140 cm^{-1} during CPE of $\mathbf{2}^{2+}$ (Figures S15(b) and S15(c)).

IR spectra recorded during the CPE of $\mathbf{2}^{2+}$ at −1.82 V (versus $Fc^{+/0}$) under CO_2 (0.28 M) display the evolution of clearly visible bands at 1735, 1612 and 1272 cm^{-1} along with those of the CO_3^{2-} byproduct (Figures 5b and S12(b)). The 1735 cm^{-1} band can be explained by a C=O stretching vibration in either $[\mathbf{2}\text{-}CO_2]^0$ or $[\mathbf{2}^{tp}\text{-}CO_2CO_2]^{0,c}$; (calc: 1729 cm^{-1} and 1760 cm^{-1}, respectively; (Figures S18(a) and S18(c)), while no absorption is expected for $[\mathbf{2}^{tp}\text{-}CO_2CO_2]^{-1,c}$ in this range according to its DFT calculated IR spectrum (Figures S18(d). The experimental IR band at 1272 cm^{-1} corresponds very well to computed C–O stretches at 1253 cm^{-1} and 1291 cm^{-1} for $[\mathbf{2}^{tp}\text{-}CO_2CO_2]^{0,c}$ and $[\mathbf{2}^{tp}\text{-}CO_2CO_2]^{-1,c}$ respectively (Figures S18(c) and S18(d)[79]), while the experimentally obtained peak at 1612 cm^{-1} is only found in the calculated IR spectrum of $[\mathbf{2}^{tp}\text{-}CO_2CO_2]^{-1,c}$ at 1614 cm^{-1} (Figures 5b and S18(d)). This unique absorption allows for the identification of $[\mathbf{2}^{tp}\text{-}CO_2CO_2]^{-1,c}$ as one of the intermediates accumulated during CPE. Thus, the IR monitoring indicates the presence of $[\mathbf{2}\text{-}CO_2]^0$, $[\mathbf{2}^{tp}\text{-}CO_2CO_2]^{0,c}$ and $[\mathbf{2}^{tp}\text{-}CO_2CO_2]^{-1,c}$ being built up during CPE, consistent with the small calculated energy differences between these intermediates (3.5 kcal mol^{-1} between $[\mathbf{2}\text{-}CO_2]^0$ and $[\mathbf{2}^{tp}\text{-}CO_2CO_2]^{0,c}$; 3.0 kcal mol^{-1} between $[\mathbf{2}\text{-}CO_2]^0$ and $[\mathbf{2}^{tp}\text{-}CO_2CO_2]^{-1,c}$; Figure 4). Linear $[\mathbf{2}\text{-}CO_2CO_2]^0$ is not present in detectable amounts, as its diagnostic calculated IR absorption at 1869 cm^{-1} (Figure S18(b)) is absent from the experimental CPE monitoring (Figure S19).

Conducting CPE of $\mathbf{2}^{2+}$ under identical conditions, but with $^{13}CO_2$ gives rise to FT-IR spectra that are qualitatively similar to the ones under $^{12}CO_2$, with the expected shifts due

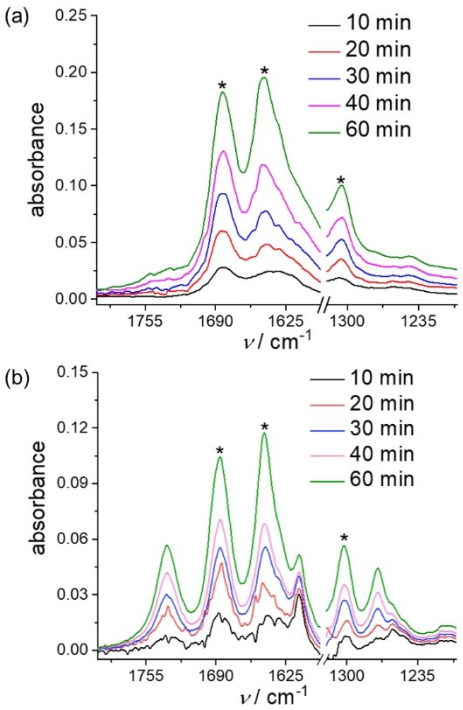

Figure 5. Fourier transformed infra-red (FT-IR) absorbance spectra of aliquots taken during controlled potential electrolysis of CO_2 saturated (0.28 M) solutions of (a) $\mathbf{1}(PF_6)_2$ (1.0 mM) and (b) $\mathbf{2}(PF_6)_2$ (1.0 mM), in anhydrous CH_3CN/0.1 M $TBAPF_6$ at an applied potential of −1.82 V (versus $Fc^{+/0}$). The peaks marked with * arise from the CO_3^{2-}.

to the isotope labelling. The C=O and C–O stretching vibrations shift by 40–50 and 15–20 cm^{-1} to lower wavenumbers,[78] respectively, when going from $^{12}CO_2$ to $^{13}CO_2$,[55,64] confirming that these IR bands arise from CO_2-derived species (Figure S20). The calculated IR bands of $[\mathbf{2}^{tp}\text{-}^{13}CO_2{}^{13}CO_2]^{-1,c}$ agree well with the experimentally observed ones from CPE (ν (cm^{-1}): experimental (calc.): 1642 (1648), 1564 (1575) and 1279 (1265) cm^{-1}, Figures S20 and S21).

The IR-spectroscopic observation of $[\mathbf{2}^{tp}\text{-}CO_2CO_2]^{-1,c}$ is consistent with a lower rate of C–O bond dissociation compared to that in $[\mathbf{1}^{bp}\text{-}CO_2CO_2]^{-1,c}$ as evidenced by a higher DFT calculated activation free energy (16.6 kcal mol^{-1} for $[\mathbf{2}^{tp}\text{-}CO_2CO_2]^{-1,c}$ versus 11.2 kcal mol^{-1} for $[\mathbf{1}^{bp}\text{-}CO_2CO_2]^{-1,c}$; Figures 3 and 4).

The highest activation energy barriers ($\Delta G^{\ddagger}$) in the pathway for $\mathbf{2}^{2+}$ (Figure 4) relative to $[\mathbf{2}\text{-}CO_2]^0$ are associated with the cleavage of C–O bond in $[\mathbf{2}^{tp}\text{-}CO_2CO_2]^{-1,c}$ at 19.6 kcal mol^{-1} and the release of CO_3^{2-} at 19.1 kcal mol^{-1}. The barriers correspond quite well with the experimental catalytic rate constant k_{cat} (or maximum turnover frequency (TOF_{max})) of 0.85 s^{-1}, obtained using Foot-Of-the-Wave-Analysis (FOWA)[80,81] (Figures S22(a) and S22(b); see Supporting Information for details). The rate constant of 0.85 s^{-1} translates to a free energy barrier of 17.5 kcal mol^{-1} (calculated using the Eyring equation[76] as described earlier for $\mathbf{1}^{2+}$), which differs from the DFT calculated barrier by merely 2.1 kcal mol^{-1}. Therefore, the trend in the experimental catalytic rates of $\mathbf{1}^{2+} > \mathbf{2}^{2+}$ agree very well with the corresponding trends in their DFT calculated activation barriers (Figures 3 and 4). The deduction of k_{cat} allowed us to construct the Tafel plots of log(TOF) versus overpotential (η) (Figure S22(c)) for $\mathbf{1}^{2+}$ and $\mathbf{2}^{2+}$. This provided log(TOF_0) (TOF_0 = turnover frequency at zero overpotential) as -7.64 s^{-1} and -8.20 s^{-1} for $\mathbf{1}^{2+}$[57] and $\mathbf{2}^{2+}$ respectively.

The metallacyclic intermediate proposed in the current study is further supported by comparison with the reported IR spectrum of complex $[Ir(PMe_3)_3(Cl)(COOCOO)]$[65] (Figure S7), which possesses a similar metallacycle consisting of two CO_2 molecules in a "head-to-tail" arrangement.[65] This reference complex was prepared by the stoichiometric reaction of a low-valent metal precursor and CO_2, and exhibited IR bands at 1725, 1680, 1648 (sh), 1605, and 1290 cm^{-1},[65] which are almost identical to the IR signature of $[\mathbf{2}^{tp}\text{-}CO_2CO_2]^{-1,c}$ (Figures 5b and S18(d)).

Conclusion

In summary, the present work describes an unexplored mechanistic pathway for low-energy C–O bond cleavage in the reductive disproportionation of CO_2 to CO and CO_3^{2-}. Computational work in conjunction with IR spectroscopic detection of accumulated reaction intermediates established the involvement of an unprecedented 5-membered metallacyclic intermediate in the catalytic cycle, after ruling out alternative pathways. The formation of the metallacycle is enabled by the flexible ligation of the polypyridyl ligands, and it is shown that the ligand with the least binding strength to the metal is the one that partially de-coordinates to liberate the coordination site required for metallacycle formation.

The Ru center plays a dual role in the catalytic cycle: it acts as a Lewis base and attacks the first CO_2 molecule at an early stage of the cycle, while also acting as an intramolecular Lewis acidic site to stabilize the negative charge of the $[\mathbf{Ru}\text{-}CO_2CO_2]^0$, thereby leading to the cyclic $[\mathbf{Ru}\text{-}CO_2CO_2]^{0,c}$. The latter intermediate is crucial for energy-conserving turnover, as it allows for a third reduction at a more positive potential than that of the starting complexes $\mathbf{1}^{2+}$ and $\mathbf{2}^{2+}$. The thereby produced $[\mathbf{Ru}\text{-}CO_2CO_2]^{-1,c}$ contains structural features that allow for relatively facile C–O bond cleavage with the calculated activation barrier for this step being dramatically decreased as compared to that required for C–O bond cleavage in the non-cyclic $[\mathbf{Ru}\text{-}CO_2CO_2]^0$. Subsequent release of products closes the catalytic cycle, and gives the catalyst a good overall stability.

Considering its simplicity, it may well be that similar species in other mononuclear catalysts have hitherto been overlooked. At the same time, its identification and operation offer a new design feature that can now be implemented consciously in future catalyst designs.

Acknowledgements

The authors would like to acknowledge the Swedish National Infrastructure for Computing (SNIC), which is funded by the Swedish Research Council (VR) through grant agreement no. 2016–07213, in Linköping (NSC), for the computational resources. The computations were performed under project numbers SNIC2017/1-13, SNIC2018/3-1. SNIC2019/3-6, SNIC2020/5-41, and NAISS2023-22-89. We acknowledge NordForsk foundation (No. 85378) for the Nordic University hub NordCO_2. MA has been supported by the Swedish Research Council (VR) grant number 2018–05396, and the Knut & Alice Wallenberg (KAW) project CATSS (KAW 2016.0072). XC acknowledges the China Scholarship Council (CSC). HA and SO acknowledge the Swedish Energy Agency (grant number: 42029-1) for financial support. HA acknowledges the Cleve, Gahn and Svanberg funds from Uppsala University, Sweden, for financing the upgrading of Fourier-Transformed-Infrared-Spectrometer (FTIR) for spectroelectrochemistry. HA also acknowledges Technical University of Munich (TUM) for providing the necessary resources to finish the research work. Open Access funding enabled and organized by Projekt DEAL.

Conflict of Interest

The authors declare no conflict of interest.

Data Availability StatementReferences

The data that support the findings of this study are available in the supplementary material of this article.

Keywords: CO_2 Reduction · Electrocatalysis · Metallacyclic Intermediates · Overpotential · Polypyridyl Ligands

[1] C. Costentin, S. Drouet, M. Robert, J.-M. Savéant, *J. Am. Chem. Soc.* **2012**, *134*, 11235–11242.
[2] I. Azcarate, C. Costentin, M. Robert, J.-M. Savéant, *J. Am. Chem. Soc.* **2016**, *138*, 16639–16644.
[3] C. Costentin, S. Drouet, M. Robert, J.-M. Savéant, *Science* **2012**, *338*, 90–94.
[4] R. Francke, B. Schille, M. Roemelt, *Chem. Rev.* **2018**, *118*, 4631–4701.
[5] F. Franco, M. F. Pinto, B. Royo, J. Lloret-Fillol, *Angew. Chem. Int. Ed.* **2018**, *57*, 4603–4606; *Angew. Chem.* **2018**, *130*, 4693–4696.
[6] S. Fernández, F. Franco, C. Casadevall, V. Martin-Diaconescu, J. M. Luis, J. Lloret-Fillol, *J. Am. Chem. Soc.* **2020**, *142*, 120–133.
[7] M. L. Clark, P. L. Cheung, M. Lessio, E. A. Carter, C. P. Kubiak, *ACS Catal.* **2018**, *8*, 2021–2029.
[8] B. Merillas, E. Cuéllar, A. Diez-Varga, T. Torroba, G. García-Herbosa, S. Fernández, J. Lloret-Fillol, J. M. Martín-Alvarez, D. Miguel, F. Villafañe, *Inorg. Chem.* **2020**, *59*, 11152–11165.
[9] P. Gerschel, A. L. Cordes, S. Bimmermann, D. Siegmund, N. Metzler-Nolte, U.-P. Apfel, *Z. Anorg. Allg. Chem.* **2021**, *647*, 968–977.
[10] S. Sung, D. Kumar, M. Gil-Sepulcre, M. Nippe, *J. Am. Chem. Soc.* **2017**, *139*, 13993–13996.
[11] M. Merrouch, M. Benvenuti, M. Lorenzi, C. Léger, V. Fourmond, S. Dementin, *JBIC J. Biol. Inorg. Chem.* **2018**, *23*, 613–620.
[12] H. Dobbek, V. Svetlitchnyi, L. Gremer, R. Huber, O. Meyer, *Science* **2001**, *293*, 1281–1285.
[13] M. Can, F. A. Armstrong, S. W. Ragsdale, *Chem. Rev.* **2014**, *114*, 4149–4174.
[14] N. Elgrishi, M. B. Chambers, X. Wang, M. Fontecave, *Chem. Soc. Rev.* **2017**, *46*, 761–796.
[15] S. Dey, T. K. Todorova, M. Fontecave, V. Mougel, *Angew. Chem. Int. Ed.* **2020**, *59*, 15726–15733; *Angew. Chem.* **2020**, *132*, 15856–15863.
[16] M. E. Ahmed, A. Rana, R. Saha, S. Dey, A. Dey, *Inorg. Chem.* **2020**, *59*, 5292–5302.
[17] E. Boutin, L. Merakeb, B. Ma, B. Boudy, M. Wang, J. Bonin, E. Anxolabéhère-Mallart, M. Robert, *Chem. Soc. Rev.* **2020**, *49*, 5772–5809.
[18] T. Fogeron, T. K. Todorova, J.-P. Porcher, M. Gomez-Mingot, L.-M. Chamoreau, C. Mellot-Draznieks, Y. Li, M. Fontecave, *ACS Catal.* **2018**, *8*, 2030–2038.
[19] T. Fogeron, P. Retailleau, M. Gomez-Mingot, Y. Li, M. Fontecave, *Organometallics* **2019**, *38*, 1344–1350.
[20] A. Mouchfiq, T. K. Todorova, S. Dey, M. Fontecave, V. Mougel, *Chem. Sci.* **2020**, *11*, 5503–5510.
[21] S. Gonell, J. Lloret-Fillol, A. J. M. Miller, *ACS Catal.* **2021**, *11*, 615–626.
[22] S. Gonell, M. D. Massey, I. P. Moseley, C. K. Schauer, J. T. Muckerman, A. J. M. Miller, *J. Am. Chem. Soc.* **2019**, *141*, 6658–6671.
[23] S. Gonell, E. A. Assaf, K. D. Duffee, C. K. Schauer, A. J. M. Miller, *J. Am. Chem. Soc.* **2020**, *142*, 8980–8999.
[24] S. L. Hooe, J. M. Dressel, D. A. Dickie, C. W. Machan, *ACS Catal.* **2020**, *10*, 1146–1151.
[25] S. L. Hooe, J. J. Moreno, A. G. Reid, E. N. Cook, C. W. Machan, *Angew. Chem. Int. Ed.* **2022**, *61*, e202109645; *Angew. Chem.* **2022**, *134*, e202109645.
[26] A. W. Nichols, S. Chatterjee, M. Sabat, C. W. Machan, *Inorg. Chem.* **2018**, *57*, 2111–2121.
[27] J. J. Moreno, S. L. Hooe, C. W. Machan, *Inorg. Chem.* **2021**, *60*, 3635–3650.
[28] R. Bonetto, R. Altieri, M. Tagliapietra, A. Barbon, M. Bonchio, M. Robert, A. Sartorel, *ChemSusChem* **2020**, *13*, 4111–4120.
[29] L. Rotundo, C. Garino, E. Priola, D. Sassone, H. Rao, B. Ma, M. Robert, J. Fiedler, R. Gobetto, C. Nervi, *Organometallics* **2019**, *38*, 1351–1360.
[30] C. Cometto, L. Chen, E. Anxolabéhère-Mallart, C. Fave, T.-C. Lau, M. Robert, *Organometallics* **2019**, *38*, 1280–1285.
[31] C. Cometto, L. Chen, P.-K. Lo, Z. Guo, K.-C. Lau, E. Anxolabéhère-Mallart, C. Fave, T.-C. Lau, M. Robert, *ACS Catal.* **2018**, *8*, 3411–3417.
[32] A. Maurin, C.-O. Ng, L. Chen, T.-C. Lau, M. Robert, C.-C. Ko, *Dalton Trans.* **2016**, *45*, 14524–14529.
[33] L. Chen, Z. Guo, X.-G. Wei, C. Gallenkamp, J. Bonin, E. Anxolabéhère-Mallart, K.-C. Lau, T.-C. Lau, M. Robert, *J. Am. Chem. Soc.* **2015**, *137*, 10918–10921.
[34] C. Costentin, M. Robert, J.-M. Savéant, A. Tatin, *Proc. Natl. Acad. Sci. USA* **2015**, *112*, 6882–6886.
[35] C. Costentin, G. Passard, M. Robert, J.-M. Savéant, *J. Am. Chem. Soc.* **2014**, *136*, 11821–11829.
[36] N. Queyriaux, K. Abel, J. Fize, J. Pécaut, M. Orio, L. Hammarström, *Sustainable Energy Fuels* **2020**, *4*, 3668–3676.
[37] F. Franco, C. Cometto, L. Nencini, C. Barolo, F. Sordello, C. Minero, J. Fiedler, M. Robert, R. Gobetto, C. Nervi, *Chem. Eur. J.* **2017**, *23*, 4782–4793.
[38] K. T. Ngo, M. McKinnon, B. Mahanti, R. Narayanan, D. C. Grills, M. Z. Ertem, J. Rochford, *J. Am. Chem. Soc.* **2017**, *139*, 2604–2618.
[39] J. Agarwal, T. W. Shaw, H. F. Schaefer, A. B. Bocarsly, *Inorg. Chem.* **2015**, *54*, 5285–5294.
[40] S. E. Tignor, T. W. Shaw, A. B. Bocarsly, *Dalton Trans.* **2019**, *48*, 12730–12737.
[41] P. Gotico, L. Roupnel, R. Guillot, M. Sircoglou, W. Leibl, Z. Halime, A. Aukauloo, *Angew. Chem. Int. Ed.* **2020**, *59*, 22451–22455; *Angew. Chem.* **2020**, *132*, 22637–22641.
[42] J. A. Buss, D. G. VanderVelde, T. Agapie, *J. Am. Chem. Soc.* **2018**, *140*, 10121–10125.
[43] P. Sen, B. Mondal, D. Saha, A. Rana, A. Dey, *Dalton Trans.* **2019**, *48*, 5965–5977.
[44] D. Z. Zee, M. Nippe, A. E. King, C. J. Chang, J. R. Long, *Inorg. Chem.* **2020**, *59*, 5206–5217.
[45] M. Loipersberger, D. Z. Zee, J. A. Panetier, C. J. Chang, J. R. Long, M. Head-Gordon, *Inorg. Chem.* **2020**, *59*, 8146–8160.
[46] M. H. Rønne, D. Cho, M. R. Madsen, J. B. Jakobsen, S. Eom, É. Escoudé, H. C. D. Hammershøj, D. U. Nielsen, S. U. Pedersen, M.-H. Baik, T. Skrydstrup, K. Daasbjerg, *J. Am. Chem. Soc.* **2020**, *142*, 4265–4275.
[47] C. G. Margarit, C. Schnedermann, N. G. Asimow, D. G. Nocera, *Organometallics* **2019**, *38*, 1219–1223.
[48] M. R. Madsen, J. B. Jakobsen, M. H. Rønne, H. Liang, H. C. D. Hammershøj, P. Nørby, S. U. Pedersen, T. Skrydstrup, K. Daasbjerg, *Organometallics* **2020**, *39*, 1480–1490.
[49] S. Amanullah, P. Saha, A. Nayek, M. E. Ahmed, A. Dey, *Chem. Soc. Rev.* **2021**, *50*, 3755–3823.
[50] S. Roy, B. Sharma, J. Pécaut, P. Simon, M. Fontecave, P. D. Tran, E. Derat, V. Artero, *J. Am. Chem. Soc.* **2017**, *139*, 3685–3696.
[51] E. Haviv, D. Azaiza-Dabbah, R. Carmieli, L. Avram, J. M. L. Martin, R. Neumann, *J. Am. Chem. Soc.* **2018**, *140*, 12451–12456.

[52] S. Sung, X. Li, L. M. Wolf, J. R. Meeder, N. S. Bhuvanesh, K. A. Grice, J. A. Panetier, M. Nippe, *J. Am. Chem. Soc.* **2019**, *141*, 6569–6582.
[53] M. Hammouche, D. Lexa, M. Momenteau, J. M. Saveant, *J. Am. Chem. Soc.* **1991**, *113*, 8455–8466.
[54] I. Bhugun, D. Lexa, J.-M. Savéant, *J. Phys. Chem.* **1996**, *100*, 19981–19985.
[55] M. D. Sampson, C. P. Kubiak, *J. Am. Chem. Soc.* **2016**, *138*, 1386–1393.
[56] B. A. Johnson, S. Maji, H. Agarwala, T. A. White, E. Mijangos, S. Ott, *Angew. Chem. Int. Ed.* **2016**, *55*, 1825–1829; *Angew. Chem.* **2016**, *128*, 1857–1861.
[57] B. A. Johnson, H. Agarwala, T. A. White, E. Mijangos, S. Maji, S. Ott, *Chem. Eur. J.* **2016**, *22*, 14870–14880.
[58] S. Nishigaki, H. Yoshioka, K. Nakatsu, *Acta Crystallogr. Sect. B* **1978**, *34*, 875–879.
[59] L. L. Merritt, E. Schroeder, *Acta Crystallogr.* **1956**, *9*, 801–804.
[60] A. Gennaro, A. A. Isse, E. Vianello, *J. Electroanal. Chem. Interfacial Electrochem.* **1990**, *289*, 203–215.
[61] Z. Chen, C. Chen, D. R. Weinberg, P. Kang, J. J. Concepcion, D. P. Harrison, M. S. Brookhart, T. J. Meyer, *Chem. Commun.* **2011**, *47*, 12607–12609.
[62] J. Agarwal, E. Fujita, H. F. Schaefer, J. T. Muckerman, *J. Am. Chem. Soc.* **2012**, *134*, 5180–5186.
[63] B. P. Sullivan, C. M. Bolinger, D. Conrad, W. J. Vining, T. J. Meyer, *J. Chem. Soc. Chem. Commun.* **1985**, 1414–1416.
[64] C. W. Machan, S. A. Chabolla, J. Yin, M. K. Gilson, F. A. Tezcan, C. P. Kubiak, *J. Am. Chem. Soc.* **2014**, *136*, 14598–14607.
[65] T. Herskovitz, L. J. Guggenberger, *J. Am. Chem. Soc.* **1976**, *98*, 1615–1616.
[66] P. M. Jurd, H. L. Li, M. Bhadbhade, L. D. Field, *Organometallics* **2020**, *39*, 2011–2018.
[67] M. Feller, U. Gellrich, A. Anaby, Y. Diskin-Posner, D. Milstein, *J. Am. Chem. Soc.* **2016**, *138*, 6445–6454.
[68] J. Langer, W. Imhof, M. J. Fabra, P. García-Orduña, H. Görls, F. J. Lahoz, L. A. Oro, M. Westerhausen, *Organometallics* **2010**, *29*, 1642–1651.
[69] R. Kempe, J. Sieler, D. Walther, J. Reinhold, K. Rommel, *Z. Anorg. Allg. Chem.* **1993**, *619*, 1105–1110.
[70] L. Dahlenburg, C. Prengel, *J. Organomet. Chem.* **1986**, *308*, 63–71.
[71] E. Carmona, F. Gonzalez, M. L. Poveda, J. M. Marin, J. L. Atwood, R. D. Rogers, *J. Am. Chem. Soc.* **1983**, *105*, 3365–3366.
[72] F. Lucarini, J. Fize, A. Morozan, M. Marazzi, M. Natali, M. Pastore, V. Artero, A. Ruggi, *Sustainable Energy Fuels* **2020**, *4*, 589–599.
[73] J. J. Leung, J. Warnan, K. H. Ly, N. Heidary, D. H. Nam, M. F. Kuehnel, E. Reisner, *Nat. Catal.* **2019**, *2*, 354–365.
[74] S. Aroua, T. K. Todorova, V. Mougel, P. Hommes, H.-U. Reissig, M. Fontecave, *ChemCatChem* **2017**, *9*, 2099–2105.
[75] H. Eyring, *Chem. Rev.* **1935**, *17*, 65–77.
[76] Q. Teng, H. V. Huynh, *Inorg. Chem.* **2014**, *53*, 10964–10973.
[77] S. C. Cheng, C. A. Blaine, M. G. Hill, K. R. Mann, *Inorg. Chem.* **1996**, *35*, 7704–7708.
[78] C. Jegat, M. Fouassier, M. Tranquille, J. Mascetti, I. Tommasi, M. Aresta, F. Ingold, A. Dedieu, *Inorg. Chem.* **1993**, *32*, 1279–1289.
[79] The remaining calculated peaks at 1695 cm^{-1} and 1291 cm^{-1} for $[\mathbf{2}\text{-}CO_2CO_2]^{-1,c}$ are masked by the CO_3^{2-}/HCO_3^{2-} IR bands centered at 1686 cm^{-1} and 1301 cm^{-1}.
[80] V. C. C. Wang, B. A. Johnson, *ACS Catal.* **2019**, *9*, 7109–7123.
[81] C. Costentin, J.-M. Savéant, *ChemElectroChem* **2014**, *1*, 1226–1236.

Manuscript received: December 19, 2022
Accepted manuscript online: February 17, 2023
Version of record online: March 10, 2023